Seismicity during and after stimulation of a 6.1 km deep Enhanced Geothermal System in Helsinki, Finland

Maria Leonhardt[1], Grzegorz Kwiatek[1], Patricia Martínez-Garzón[1], Marco Bohnhoff[1,2], Tero Saarno[3], Pekka Heikkinen[4], and Georg Dresen[1,5]

5 [1]Helmholtz Centre Potsdam, GFZ German Research Centre for Geosciences, Section 4.2: Geomechanics and Scientific Drilling, Potsdam, Germany, [2]Department of Earth Sciences, Free University of Berlin, Berlin, Germany, [3]St1 Deep Heat Oy, Helsinki, Finland, [4]Department of Geosciences and Geography, University of Helsinki, Helsinki, Finland, [5]Institute of Earth and Environmental Sciences, University of Potsdam, Potsdam, Germany

10 *Correspondence to*: Maria Leonhardt (maria.leonhardt@gfz-potsdam.de)

Abstract. In this study, we present a high-resolution dataset of seismicity framing the stimulation campaign of a 6.1 km deep Enhanced Geothermal System (EGS) in Helsinki suburban area and discuss the complexity of fracture network development. Within St1 Deep Heat project, 18,160 m^3 of water was injected over 49 days in summer 2018. The seismicity was monitored by a seismic network of near-surface borehole sensors framing the EGS site 15 in combination with a multi-level geophone array located at ≥ 2 km depth. We expand the original catalog of Kwiatek et al. (2019) including detected seismic events and earthquakes that occurred two month after the end of injection, totaling to 61,163 events. We relocated events of the catalog with moment magnitudes between M_W -0.5 and M_W 1.9 using the double-difference technique and a new velocity model derived from a post-stimulation vertical seismic profiling campaign. The analysis of the fault network development at reservoir depth of 4.5-7 km 20 is one primary focus of this study. To achieve this, we investigate 191 focal mechanisms of the induced seismicity using a cross-correlation based technique. Our results indicate that seismicity occurred in three spatially separated clusters centered around the injection well. We observe a spatio-temporal migration of the seismicity during the stimulation starting from the injection well in northwest (NW) - southeast (SE) direction and in northeast (NE) direction towards greater depth. The spatial evolution of the cumulative seismic moment, the distribution of events 25 with $M_W \geq 1$ and the fault plane orientations of focal mechanisms indicate an active network of at least three NW-SE to NNW-SSE orientated permeable zones which is interpreted to be responsible for migration of seismic activity away from the injection well. Fault plane solutions of the best-constrained focal mechanisms as well as results for the local stress field orientation indicate a reverse faulting regime and suggest that seismic slip occurred on a sub-parallel network of pre-existing weak fractures favorably oriented with the stress field, striking NNW-30 SEE with a dip of 45° ENE, parallel to the injection well.

1 Introduction

Deep geothermal energy is considered as a potential source of low CO_2-emission energy to replace fossil fuels. The successful development of deep geothermal reservoirs is crucial for the economic production of hot fluids for energy production. However, crystalline basement rocks hosting deep geothermal reservoirs in general are low-porosity and low-permeability formations. In Enhanced Geothermal Systems (EGS) hydraulic stimulation with massive fluid injection is applied to improve reservoir permeability (e.g. Giardini, 2009). Fluid injection at depth in EGS stimulations and in waste-water disposal is commonly associated with induced seismicity (e.g. Ellsworth, 2013; Majer et al., 2012). Successful mitigation of induced seismic hazard is important for public acceptance of geothermal projects as significant concern exists related to the occurrence of larger induced earthquakes during previous EGS projects, e.g. in Basel and St. Gallen, Switzerland (e.g. Giardini, 2009; Diehl et al., 2017) or most recently in Pohang, South Korea (Hofmann et al., 2019; Ellsworth et al., 2019).

A well-designed seismic network is pre-requisite for high-resolution data acquisition, real-time seismic monitoring and analysis of induced seismicity (e.g. Bohnhoff et al., 2018). Subsequent feeding of seismic data into a traffic-light-system (TLS) may substantially contribute to mitigate the associated seismic hazard and risk. A successful and safe approach to stimulation of the world's deepest EGS in the metropolitan area of Helsinki was recently presented by Kwiatek et al. (2019). Over 49 days in summer 2018, the St1 Deep Heat Company injected more than 18,000 m³ of water at 6.1 km depth. A M 2.1 red alert threshold of the TLS defined by the local authorities was successfully avoided by a careful adjustment of the hydraulic energy input in response to real-time monitoring of the spatio-temporal evolution of seismicity. The largest seismic event was confined to a moment magnitude of M_W 1.9 (Ader et al., 2019; Kwiatek et al., 2019).

High quality state-of-the art analysis of induced seismic waveform data is crucial for a detailed reservoir characterization (Kwiatek et al., 2013). High precision locations of hypocenters are typically obtained by applying relocation techniques such as the double-difference method (Waldhauser and Ellsworth, 2000). Using relocated data, a precise spatio-temporal evolution of induced seismicity can be tracked providing insight in fluid migration pathways in the reservoir (e.g. Kwiatek et al., 2015; Diehl et al., 2017). In addition, seismic source parameters such as seismic moment and source size provide crucial insights into the fracture network geometry.

Bentz et al. (2020) recently showed that many EGS fluid injections display an extended period of stable evolution of the cumulative seismic moment. Following Galis et al. (2015), this indicates the growth of self-arrested ruptures, in contrast to unstable increase of seismic moment resulting in runaway ruptures that are only limited by the size of tectonic faults. Thus, unusual trends or potential changes in the seismic moment evolution may provide information on growth and activation of ruptures and thus also on the anthropogenic seismic hazard

and subsequent risk. For example, Bentz et al. (2020) observed a steep and not stabilizing increase of the cumulative seismic moment potentially signifying unbound rupture propagation during stimulation for the Pohang EGS project. Dynamic source characteristics of seismic events including radiated energy, stress drop and apparent stress allow the evaluation of seismic injection efficiency (Maxwell, 2008) and the estimation of the energy budget of a stimulation campaign. Moreover, focal mechanisms provide important information for hazard assessment, as they can illuminate activation of large pre-existing structures such as major and potentially critically pre-stressed faults (e.g. Deichmann and Giardini, 2009; Ellsworth et al., 2019). Using focal mechanisms, Ellsworth et al. (2019) showed that induced seismicity activated a fault zone which ultimately triggered the large M_W 5.5 earthquake at Pohang. The authors suggested that seismic analysis performed during stimulation sequences may provide early information on increasing seismic hazard. In addition, stress tensor inversion of focal mechanism data using e.g. the *MSATSI* (Martínez-Garzón et al., 2014) or *BRTMF* (D'Auria and Massa, 2015) approaches allow the estimation of potential changes of the local stress field but require high-quality seismic waveform data from dense local seismic networks. Studies of the spatial and temporal variations of the stress field orientation contribute to understanding complex seismo-mechanical processes occurring in the reservoir during injection (Kwiatek et al., 2013). Martínez-Garzón et al. (2013) first observed a clear correlation of temporal stress changes in response to high injection rates at The Geysers geothermal field.

In this study we present a refined high-resolution dataset of seismicity induced during stimulation of the world's deepest geothermal EGS in the Helsinki suburban area in 2018 (Kwiatek et al., 2019; Ader et al., 2019; Hillers et al., 2020). The data was collected using a combined seismic network of individual sensors in shallow boreholes framing the injection site combined with a multi-level vertical geophone array at ≥2 km depth. Our dataset expands, refines and completes the original study of Kwiatek et al. (2019). We include seismic events which occurred after the end of the hydraulic stimulation and refine the seismic catalog using double-difference relocation with a new velocity model derived from a post-injection Vertical Seismic Profiling (VSP) campaign. To analyze the structural complexity of the reservoir, we investigate the spatio-temporal seismicity evolution and the temporal as well as spatial distribution of the seismic moment release during and after stimulation. This analysis is supported by an extensive catalog of source mechanisms derived from a cross-correlation based technique. Information on the local stress field orientation is derived from seismicity data. We discuss the evolution of potentially permeable zones in the reservoir and the re-activation of a network of small-scale fractures during and after stimulation.

2   Methodology

Expanding the study of Kwiatek et al. (2019), we enhanced, reprocessed and relocated the original seismic catalog now also including post-injection events between July 22nd and September 24th. During and after the stimulation, induced seismicity was monitored by a dense seismic network of three-component sensors consisting of a 12-level vertical borehole array as well as 12 near-surface seismometers with full azimuthal coverage. The borehole array with 15 Hz sensors, sampled at 2 kHz, was installed at a depth from 1.95 to 2.37 km in the monitoring well *OTN-2* close to the injection well *OTN-3* whereas the 4.5 kHz near-surface seismometers, sampled at 500 Hz, were placed in wells with depths between 0.3 to 1.15 km and lateral distances of 0.6 to 8.2 km around the injection well (Fig. 1).

The reprocessed seismic catalog with description of its properties is available as separate data publication (see section *data availability*) and consists of 5,456 events with $M_W \geq$ -2.47 that were detected and located during and after the stimulation (industrial monitoring) and reprocessed in our study. A total of 55,707 ~~smaller~~ events with $M_W \geq$ -0.95 were further detected during and after the stimulation but were not located or processed later on. These were also included in published seismic catalog. For further explanation about the original seismic catalog see Kwiatek et al. (2019).

2.1 Hypocenter locations

The enhanced sub-catalog of 5,456 events including 946 post-stimulation events was reprocessed applying a new updated 1D layered velocity model developed from P-wave onset times of calibration shots obtained during a post-injection VSP campaign (Fig. S1, see also data publication). Due to a low Signal-to-Noise (S/N) ratio of the VSP data, the S-wave arrival times could not be determined. Thus, the V_P/V_S ratio was optimized by a trial-and-error procedure, where we ultimately constrained a V_P/V_S ratio of 1.71 that minimized the cumulative residual errors of all located events, and at the same time kept the first induced events close to corresponding injection well *OTN-3*.

The hypocenter locations were estimated using the Equal Differential Time (EDT) method (Zhou, 1994; Font et al., 2004; Lomax, 2005) and the new VSP-derived velocity model. In addition, station corrections were applied. The minimization of travel time residuals:

$$\left\| \left(T_j^{th} - T_i^{th} \right) - \left(T_j^{obs} - T_i^{obs} \right) \right\|_{L_2} = min, \tag{1}$$

where T^{th} and T^{obs} are all unique pairs (i,j) of theoretical and observed travel times of P- and S-phases, were resolved using the Simplex algorithm (Nelder and Mead, 1965; Lagarias et al., 1998) . A total of 2,958 reprocessed events were located around the injection well *OTN-3* at an epicentral distance of less than 5 km and at depth of 4.5 to 7 km. The hypocenters of these events were included to the reprocessed and published data catalog.

To further refine the quality of hypocenter locations, 2,178 from the 2,958 absolute located events with at least 10 P-wave and 4 S-wave picks were selected and the double-difference relocation technique (hypoDD) was applied using the new VSP-derived velocity model (Waldhauser and Ellsworth, 2000). An iterative least-square inversion was used to minimize residuals of observed and predicted travel time differences for event pairs calculated from the existing P- and S-wave picks of the selected catalog data. The residuals were minimized in ten iterations steps. For the last iteration, the maximum threshold for travel time residuals were set to 0.08 s and the maximum distance between the catalog linked event pairs was defined as 170 m. With the hypoDD method 1,986 events were relocated and thus 91 % of the selected 2,178 events. The residuals of the relocations have a root mean square error of 9 ms. The relocation uncertainties were then assessed using a bootstrap technique (Waldhauser and Ellsworth, 2000; Efron, 1982) leading to relative location precision not exceeding ±52 m for 95 % of the catalog.

2.2 Source mechanisms

To address the structural complexity of the reservoir in close proximity of the injection borehole below 4.5 km depth, source mechanisms were determined for a selected subset of events. For the 63 events with largest moment magnitudes located within the main (deepest) hypocenter cluster we first manually picked the P-wave onset polarities on the vertical component seismograms of all available stations. All waveforms were first filtered with a second order 120 Hz low-pass Butterworth filter. The same approach was applied to the 25 strongest events of the two shallower hypocenter clusters (see Fig. 3). The focal mechanisms (FMs) were determined using the *HASH* software (Hardebeck and Shearer, 2002). For each fault plane solution (FPS), associated uncertainties in a form of *acceptable* solutions are provided, calculated by perturbing take-off angles and azimuths by up to 3° (95 % confidence interval) to simulate the hypocenter location and velocity model uncertainties, respectively.

Aiming at increasing the catalog of focal mechanisms, we extended the focal mechanism calculations to smaller events with lower S/N ratio using the cross-correlation-based technique of Shelly et al. (2016). Additional 297 small events with lower S/N ratio were processed. To this end, the waveforms from a *template* set of 70 events with manually picked P-wave polarities were used to recover relative polarities of a *target* set of waveforms from 297 events, including 45 post-stimulation events and 18 events with manually-picked polarities. The waveforms of the events of both sets were first pre-processed focusing on the P-wave polarities obtained from the vertical components of all available stations. Seismograms were filtered with a second order 120 Hz low-pass Butterworth filter and a window length of 0.064 s including 0.012 s before the P-wave first motion. After a few trials, the low-pass Butterworth filter was fixed to 80 Hz for three stations of the satellite network due to a higher quality of the estimated polarity results for these stations. Considering the stations separately, each extracted waveform from the *target* set was cross-correlated with all remaining waveforms forming the *template* set. This resulted, for a

particular station and *target* event, in a vector of 70 cross-correlation (CC) coefficients with the sign representing the relative polarities between *target* and *template* P-wave onsets for a particular station. Following Shelly et al. (2016), if the lag time of the largest cross-correlation peak was lower than 0.2 times the extracted wavelength, the

155 CC was accepted and used as a relative polarity estimation between *target* event and *template*. The polarity estimates obtained from the CC values between the picked *template* and *target* events are relative and weighted by the absolute value of corresponding cross-correlation coefficient. Thus, the sign of the estimated polarity of the *target* event will be positive if the *template* and the *target* event have the same P-wave first motion.

For each station k, the vectors containing relative polarity estimates between one target event i and all

160 templates j were gathered in a i-by-j matrix. A Singular Value Decomposition (SVD) was applied to the relative estimated polarity matrix of each station k to extract the strongest common signal of any *target* event obtained by the first left singular vector of the SVD (Shelly et al., 2016; Rubinstein and Ellsworth, 2010). The estimated first left singular vectors for each station k are gathered in a i-by-k matrix

$$PP_{ik} = \begin{bmatrix} pp_{11} & \cdots & pp_{1k} \\ \vdots & \ldots & \vdots \\ pp_{i1} & \cdots & pp_{ik} \end{bmatrix}, \tag{2}$$

165 which then represents the most reasonable, however, still relative polarity pattern of each *target* event.

To reduce the polarity ambiguity of the events, we considered 18 events with known manually picked polarities included in the *target* event set. For each station k, the SVD-derived polarities of these events were compared with manually picked polarities to investigate whether the polarities have similar or opposite signs. In case of same polarities, the SVD-derived polarities of other events should also show the right sign for the particular stations.

170 Estimated polarity patterns of the events were then used to calculate focal mechanisms. For further investigation we only considered events with a good quality of estimated focal mechanisms no matter if the polarities were manually picked or estimated. Thus, we only used events with focal mechanisms that have root mean square fault plane uncertainties less or equal 35° (Hardebeck and Shearer, 2002). The final catalog of focal mechanisms includes 191 events with either manually or estimated polarity pattern and is presented with associated

175 uncertainties in the data publication (see section *data availability*).

2.3 Complexity of source mechanisms

To investigate the variability of the estimated focal mechanisms, we first calculated the principal axis directions of the double-couple seismic moment tensor derived from focal mechanism for each event. To quantify the level of similarity of any two focal mechanisms, we calculated the 3D Kagan rotation angle between principal axis

180 directions of both events (Kagan, 1991; Kagan, 2007; Tape and Tape, 2012). Low values of Kagan angle (<20°)

6

suggest that focal mechanisms of two events are similar. To further group events into families with similar source mechanisms, an unsupervised classification of the 191 events was performed using a hierarchical cluster analysis based on the similarity of estimated Kagan rotation angles. Thus, the measurement of proximity PR of any two focal mechanisms was defined as a distance metric

185 $$PR_{ij} = \frac{1-\cos(\theta_{ij}^{rot})}{1.5}, \tag{3}$$

where θ_{ij}^{rot} is a matrix containing the estimated rotation angles between any focal mechanism pair ij. In the following, the dendrogram tree based on the hierarchical clustering was used to separate focal mechanisms into different families.

To investigate the local stress field orientation in the reservoir surrounding the injection well, we applied
190 the linear stress inversion method *MSATSI* (Martínez-Garzón et al., 2014) and the Bayesian-analysis-based and nonlinear stress inversion method *BRTM* of D'Auria and Massa (2015). In both methods, the strike, dip and rake angles of the fault plane solutions from the focal mechanisms were used to invert for the orientation of three stress axes. A relative measure of the stress magnitude is obtained by the stress shape ratio R (e.g. Hardebeck and Michael, 2006; Lund and Townend, 2007)

195 $$R = \frac{\sigma_1-\sigma_2}{\sigma_1-\sigma_3}. \tag{4}$$

3 Results

3.1 Seismic catalog update

The moment magnitudes of the absolute located and relocated seismicity areis plotted with time during and after
shut-in as grey and orange dots in Fig. 2. The five different stimulation phases (P1-P5) performed in 2018 are also
200 shown in Fig. 2 in combination with the wellhead pressure and seismic event rate. Further details of the stimulation protocol and seismicity evolution are presented by Kwiatek et al. (2019), and here we focus on analysis of post-stimulation seismicity.

The 213 post-injection events with absolute locations were detected during a time period of two months
after shut-in of injection and all had magnitudes $M_W \geq -0.7$. After shut-in, the seismic event rate started to rapidly
205 decrease (Fig. 2). This decrease in activity continued until the 5th day after the end of the injection followed by a slower decrease thereafter. During the first two days after shut-in, seven events with $M_W \geq 1.0$ occurred. The largest event had a magnitude of $M_W = 1.5$ and occurred directly after bleed-off, followed closely by two M_W 1.3 events. Three events with $M_W \geq 0.9$ occurred within the first 11 days of the post-stimulation phase. Two further

7

$M_W > 1$ events occurred within 24 hours and 17 days after the stimulation ended, one with moment magnitude of 1.6 (Fig. 2). The latter events coincided with engineering operations performed in the injection well.

The updated relocated hypocenters occurred in three spatially separated clusters elongated in southeast (SE) - northwest (NW) direction and centered along the injection well, in good agreement with Kwiatek et al. (2019) (Fig. 3). Elongation of the two shallower clusters in SE-NW direction is sub-parallel to the local maximum horizontal stress $S_H^{max} = 110°$ (Kwiatek et al., 2019; Heidbach et al., 2016; Kakkuri and Chen, 1992). The main seismicity cluster centers around the open-hole section of the borehole and spans ~700 m depth (Fig. 3b). This exceeds vertical relocation precision, which is well constrained due to sensors located in a vertical borehole. The spatio-temporal seismicity evolution during the stimulation developed in two preferential directions starting from the injection well: in NW-SE direction sub-parallel to the direction of S_H^{max} as well as in northeast (NE) direction with depth. The relocated post-stimulation events are mainly located at the outer edges of the clusters following the trend observed during the stimulation. The post-injection seismicity shows no spatial migration and ~~seems to be mostly confined to three isolated clusters, with two of them located on the NW flank of the injection well *OTN-3* (Fig. 3a). T~~the largest post-stimulation events with magnitudes between M_W 1.0 and M_W 1.5 occurred at the NNW and SSE outer edge of the main cluster. These events are located in close proximity to some of the largest events of the last stimulation phase P5 (red rectangles in Fig. 3a), when high seismicity rates were observed.

3.2 Temporal evolution of cumulative seismic moment

For the stimulation period, the temporal evolution of the cumulative seismic moment release is discussed by Kwiatek et al. (2019). Here, we show the temporal evolution of the cumulative seismic moment (CM_0) release for a time period of 30 days during the post-stimulation period and compare it with the evolution before shut-in of injection. During the first two days of the post-stimulation period, the increase of CM_0 was similar to the first two days of stimulation phases P1-P5 (Fig. 4). Shortly after bleed-off, the CM_0 rapidly increased due to the three $M_W \geq 1$ events (Fig. 2). Thereafter, the increase of post-stimulation moment release was substantially less compared to a similar time period during P1-P5. Only two single events occurred with $M_W \geq 1$ during day 17, seemingly triggered by post-stimulation engineering operations in the well.

The temporal evolution of the CM_0 separated for each hypocenter cluster, marked in Fig. 3b, is shown in Fig. 5. For the upper cluster, the increase in the CM_0 is visibly larger for the stimulation phase P1 than for the other phases. For stimulation phase P2, a substantial increase in CM_0 occurred between day 4 and 5. For the central hypocenter cluster, a substantial increase in the CM_0 is visible for stimulation phase P2, P4 and P5 at the beginning of day 3 and also for P1 and P4 during day 6. For both upper and central clusters, the post-stimulation CM_0 is

substantially smaller compared to that from injection (Fig. 5a-b). The CM_0 during post-stimulation in bottom cluster is similar to P2-P5 within the first two days and afterwards lower than P2-P5 ~~for the main cluster~~. Inevitably, the bottom cluster that hosts the majority of the seismic activity also displays the highest CM_0 (Fig. S2). We note that the slopes of the CM_0 evolution are similar for the upper and central cluster, but steeper for the bottom cluster (Fig. S2).

3.3 Spatial evolution of cumulative seismic moment

For the spatial distribution of the seismic moment, the area around the injection well was separated into horizontal bins of 50x50 m. The cumulative seismic moment of all events within each bin was then investigated by disregarding the depth. During stimulation, the largest moment release and level of seismic activity occurred at the center of the main event cluster at the bottom of the injection well close to the open-hole section (Fig. 6a-b). Furthermore, larger events in the main cluster tend to locate at the greatest depths. Interestingly, a NNW-SSE alignment of enhanced cumulative seismic moment release is visible in the main hypocenter cluster in agreement with the preferred NW-SE trending direction of the two upper hypocenter clusters. The hypocenters of larger events show a similar alignment (Fig. 6a, S3). A smaller area at the NNW outer flank of the bottom hypocenter cluster displays anomalously high CM_0 release caused by large events occurring during the last injection phases and after injection (red rectangle in Fig. 6a-b). Interestingly, epicenters of two tectonic seismic events with M_W 1.4 and M_W 1.7 were reported to occur in 2013 a few kilometers NW of the bottom hole section of well *OTN-3* (Kwiatek et al., 2019).

3.4 Complexity of source mechanisms

We determined 191 single-event focal mechanisms (Fig. 7). Using the dendrogram tree based on hierarchical clustering (Fig. S4), events were separated into three distinct families (I-III) with similar focal mechanism orientations containing 99, 60 and 27 events, respectively (different coloring of beach balls in Fig. 7). Five events were not grouped in any of the three families and thus, were not considered any further. Events belonging to the three families are not separated spatially. Oblique reverse faulting is the dominant source mechanism type, which is in contrast to the regional strike slip regime (Kwiatek et al., 2019). The two largest events with reverse faulting were classified into family III. Fault plane solutions from all families indicate a range of preferred SSE-NNW to SW-NE strike directions, sharing comparable dips ranging approx. 35-50° (Fig.7a and 7e). The source mechanisms of only a few events indicate strike-slip faulting, with two of them occurring after shut-in. A total of 1~~2~~4 estimated focal mechanisms are post-stimulation events (Fig. 7b, 7d and 7f). The post-stimulation events contained in the

9

main hypocenter cluster at the bottom of the well have similar focal mechanisms as events during the stimulation. In the central hypocenter cluster, two strike-slip events occurred close by.

270   To further explore separation of the focal mechanisms into distinct families, we analyzed the rotation angle between principal P- and T-axes as a measure of mechanism (dis)similarity. We first calculated mean fault plane solution for each family. The strike/dip/rake-values of the mean fault plane solutions (FPS) for family I, II and III are 332°/47°/43° and 32°/51°/141° and 67°/36°/122°, respectively. The focal mechanisms with mean fault plane solutions and all best FPSs of each family are plotted in Fig. 8a-c. Hillers et al. (2020) recently estimated

275 focal mechanisms for the 14 largest events for which the majority is similar to family I FMs. The calculated rotation angles between mean solutions of family I and II, I and III, II and III are 71°, 59° and 53°, respectively. Taking into account that focal mechanisms are assumed to be similar if the Kagan rotation angle is less than 20°, none of the three families is similar to each other. Difference between family I and II is the most prominent, whereas rotations I-III and II-III are comparable. However, despite mean solutions of different families are

280 quantitatively distinct, the individual mechanisms are not necessarily very different (Fig. 8d-f) in between families. The total P-axis uncertainties are strongly overlapping among between three families. At the same time, the T-axes uncertainties form three distributions that, while compared between families, are only partially overlapping. This overall suggest that the FPSs may be sensitive to changes in polarities on individual stations located close to the nodal plane.

285   In the following, we analyzed qualitatively the polarity patterns of events forming three families. Regardless of manually picked or estimated polarities, tThe most repetitive polarity pattern observed at each station for a particular family is plotted in Fig. 8a-c. For each family and station, the percentage of FM events showing this repetitive pattern is presented in Tab. S1. We first verified consistency of polarity patterns for events with manually picked polarities (N=37/15/15 FPSs for family I, II, III, respectively). We noted the strike slip

290 mechanisms are attributed to least well-constrained focal mechanisms belonging to family II. The main substantial difference in the polarity patterns across families seems to be related to polarities observed at two stations *MALM* and *MUNK* (Fig. 8a-c). For family I, the polarities on these two stations are negativepositive and extremely consistent among events forming the family (35 out of 37 events display such a behavior). For family II, we observe *MALM* and *MUNK* to have mostly negative and positive polarity pattern, respectively. For family III, the

295 situation is reversed with *MALM* and *MUNK* having predominantly positive and negative polarity pattern, respectively. We further analyzed qualitatively the polarity pattern of events with polarities estimated from cross-correlation based technique of Shelly et al. (2016). Here, the situation generally further complicates due to ambiguities in resolving the polarities due to decreased signal-to-noise ratio. However, for the majority of the events forming family I, the resolved focal mechanisms still show a similar consistent polarity pattern as the most

10

300   repetitive pattern shown in Fig. 8a~~to that from manually picked ones~~, with only incidentally changing polarities on stations *UNIV* and *RUSK* located away and thus displaying lower signal-to-noise ratio. The pattern of resolved polarities for family II is generally comparable to the most repetitive polarity pattern shown in Fig. 8b~~that resolved for manual polarities~~. However, 18~~9~~ out of 45 events have negative estimated polarities for ~~*MALM* and~~ *MUNK*, thus the resolved polarity patterns seem to vary more in comparison to that of family I. The events with estimated

305   polarities for family III have the same patterns for stations *MALM* and *MUNK* as the most repetitive pattern in Fig. 8c~~the manually picked events~~ except of two~~one~~ events. However, other stations (e.g. *UNIV*, *RUSK* and *LASS*) with lower signal-to-noise ratio display sometimes varying resolved polarities for family II and III. We suppose that 1) the attribution of focal mechanism to a particular family is substantially dependent on the polarity pattern of a limited number of stations that are located close to the nodal planes, and 2) family I focal mechanisms seem the

310   most stable.

Using the *BRTM* and *MSATSI* stress tensor inversion methods based on 191 focal mechanisms, we estimated the local stress field orientation. The variability of FMs to constrain the stress field inversion is given due to high Kagan rotation angles between the mean FPSs of the three families with 53° to 71°. The *BRTM* results show that the maximum principal stress axis σ_1 is oriented almost horizontally with a trend of 279° and a plunge

315   of 4° (Fig. 9). The minimum principal stress axis σ_3 has a trend and plunge of 185° and 67°, respectively. ~~The stress shape ratio is calculated with R = 0.53.~~ The ~~estimated orientation~~ trend of σ_1 ~~deviates~~and the stress shape ratio are comparable to their independent estimates using wellbore breakouts and minifrac shut-in pressures (see Backers et al., 2016, Kwiatek et al., 2019 for details) where~~ ~10° from the local maximum horizontal stress~~ S_H^{max} = N110°E and R = 0.46 were reported ~~(Kwiatek et al., 2019)~~. Using the *MSATSI* method, the trend and plunge

320   of σ_1 is calculated with 271° and 11°, respectively. Thus, the estimated trend of σ_1 deviates ~20° from the maximum horizontal stress S_H^{max}. The minimum principal stress axis σ_3 is oriented with a trend of 76° and a plunge of 79°. The estimated stress shape ratio is with R = 0.72 larger compared with ~~the~~ respect to the *BRTM* and geophysical estimate s.

The stress obtained by focal mechanism inversion ~~of the induced seismic events~~ represents a local reverse

325   faulting regime. This is in contrast to the regional strike-slip regime estimated from regional stress and borehole data (Kwiatek et al., 2019). Only the focal mechanisms of a few events present a dominant strike-slip faulting, which typically are smaller events with a less well constrained polarity pattern.

4 Discussion

Analysis of the seismic data suggests that fluid injection was performed into a complex network of small-scale pre-existing and distributed fractures and minor faults, rather than activating a single, major fault (Kwiatek et al., 2019). In an effort to characterize the structural complexity of the reservoir in detail, we compiled a high-resolution dataset of hypocenters and single-event focal mechanisms by enhancing and refining the original seismic catalog.

The relocated events of our updated catalog show three separated spatial hypocenter clusters along the injection well in good agreement with Kwiatek et al. (2019) and Hillers et al. (2020). Hillers et al. (2020) used seismic data collected from an independent surface-based seismic network of dense sub-arrays, whereas Kwiatek et al. (2019) used the same seismic network as we do but a simplified velocity model and slightly different V_P/V_S ratio. The hypocentral depths of the events vary slightly between this and previous studies. We found that differences between absolute locations among these catalogs are likely explained by variations in V_P/V_S ratios and velocity models.

We also provide the first analysis of post-stimulation events expanding the seismic catalog to investigate potential changes in the seismicity pattern from stimulation to the post-stimulation period. Compared to the seismicity occurring during the stimulation, the post-stimulation seismicity shows no spatio-temporal migration. ~~and remains largely confined to three separate clusters. One cluster arose after bleed-off and is located at the NW flank of the central hypocenter cluster that formed during stimulation.~~ The largest post-stimulation events occurred at the NNW and SSE outer edges of the main hypocenter cluster where also anomalously higher seismicity rate and larger events were observed during the last stimulation phase P5 (cf. Fig. 3). For the main hypocenter cluster, the temporal evolution of the post-stimulation CM_0 shows similarities to the injection period until bleed-off of the well with only small changes thereafter. This suggests that seismicity is driven by the elevated pressure in the reservoir due to the previous hydraulic pumping (=increased stored elastic energy). However, hypocenter propagation requires active pumping. This is indicated by a much smaller residual increase in CM_0 and no further migration of the seismicity after bleed-off and decrease in reservoir fluid pressure.

The spatio-temporal seismicity evolution during stimulation as well as the spatial distribution of the cumulative seismic moment release indicate clear alignment of the events in NW-SE direction in the two shallower hypocenter clusters which could signify activation of permeable zones along faults or joints oriented in this direction. Existence of these zones is supported by the results of *OTN-3* well logging, where intervals of highly damaged rocks were detected that roughly coincide with the intersection of the upper seismicity clusters and the well path. For the largest bottom seismicity cluster, the relocated seismicity is distributed diffusively around the injection well. However, larger seismic events form a distinct alignment along a NNW-SSE direction (Fig. 6a, S3)

with post-stimulation events clearly located at the perimeter of the narrow zone (Fig. S3). This alignment indicates activation of another permeable zone similar to the two upper ones. The NNW-SSE trending orientation coincides with an abundance of very similar focal mechanisms from the best constrained family I events with strike direction nearly identical to the NNW-SSE alignment of hypocenters. Moreover, two natural micro-earthquakes with M_W 1.7 and M_W 1.4 occurred in 2013 a few kilometers NNW from the well (Kwiatek et al., 2019). Although there is no detailed information available on their depths due to limited coverage of the seismic network at their origin time, their epicentral location coincides with the NNW perimeter of the bottom NNW-SSE alignment hosting large induced seismicity events as well. These observations suggest that the stimulation activated at least three prominent NW-SE to NNW-SSE oriented permeable zones of subparallel fractures or faults that are responsible for seismicity migration away from the injection well during the stimulation. The deepest NNW-SSE trending zone is buried in a more disperse seismic activity forming the bottom cluster and hosts the largest induced (and likely earlier some natural) earthquakes. The fact that the largest events occurred in the deepest permeable zone may be simply related to the highest expected pore pressure perturbation in this volume due to injection and migration of fluids. Kwiatek et al. (2019) speculated that the maximum event magnitude is either limited by available fault sizes or strength of the faults. The total length of NNW-SSE trending permeable bottom zone (~650 m, Fig. S3), clearly marked by the numerous and very similar focal mechanisms, is much larger than the average size of a single M_W 2 earthquake (~80 m diameter) with even lower relocation precision. We therefore suggest that the upper limit to maximum magnitude is related to the low fault strength.

For the main hypocenter cluster, the seismicity migrates towards the NE and towards greater depths, dipping in the same direction as the inclined portion of *OTN-3* well (Fig. 3). The propagation of seismicity may signify activation of small-scale fractures striking NNW-SSE and dipping along the injection well. This is again supported by the catalog of source mechanisms forming family I events (cf. Fig. 7 and 8a). To further understand this striking observational and qualitative agreement of family I fault planes with spatial distribution and evolution of seismic activity, we tested which family of focal mechanisms is better oriented for failure within the local stress field estimated using the *BRTM* method. The resulting *BRTM* stress tensor and estimated stress shape ratio $R = 0.53$ has been used to create a Mohr diagram of the 3D stress state (Fig. 10) (cf. Vavryčuk, 2014; Martínez-Garzón et al., 2016). In the following, we projected A projection of estimated FPSs into a the Mohr circle diagram which reveals revealed fault plane orientations with respect to the stress field (Fig. 10). Optimally oriented fault planes, located generally closer to the left part of the Mohr diagram, are more likely to be activated (e.g. Vavryčuk, 2011), e.g. in a presence of enhanced pore fluid pressure, especially for weak faults. To calculate quantify the proximity to failure criterion, we assumed a friction coefficient of $\mu = 0.7$ as a mean value for faults in the Earth's crust (Vavryčuk, 2011). While projecting the selected preferred fault plane out one of the two nodal planes from each

13

fault plane solution, we used the nodal plane that displayed higher instability coefficient I (cf. Vavryčuk, 2014; Martínez-Garzón et al., 2016):

$$I = \frac{\tau + \mu(\sigma_n + 1)}{\mu + \sqrt{1+\mu^2}}, \tag{5}$$

with τ and σ_n as the normalized shear and normal tractions, respectively and μ as the friction coefficient.

395   Clearly, FPSs from family I are the most favorably oriented with respect to the local stress field (blue points and triangles in Fig. 10), as also indicated by the highest fault instability coefficients (Fig. 11S5). It turned out that the most optimally oriented fault plane is always the one trending NNW-SSE and dipping approximately in the direction of inclined portion of *OTN-3* well (indicated by P1 nodal planes in Fig. 8a). This is also confirmed by the mean solution of family I (332°/47° plane, blue P1 marker in Fig. 10) displaying the highest instability

400   (Tab. S1). However, also the fault planes represented by the auxiliary plane of the mean solution of family I are quite favorably oriented (blue P2 marker in Fig. 10). Some of the family III events are also quite favorably oriented with the stress field. We note that instabilities of auxiliary planes of mean FPSs for family I and III are similar (green and blue P2 dots in Fig. 10, Tab. S1), in agreement with their mean auxiliary nodal plane orientations of 210°/60° (P2 in Fig. 8b-c). Qualitatively, nodal planes from family II seem to be mostly unfavorably oriented with

405   the stress field (orange points and triangles in Fig. 10), as indicated by the lowest instability coefficients (Fig. 11S5). However, some P1 nodal planes are striking N-S (cf. Fig. 8b) and thus showing quite similar orientations as the P1 FPSs of family I (Fig. 8a), leading to higher instability coefficients for these planes (orange dots and triangles close to blue and green P2 marker in Fig. 10). Here, we found 19 events of family II show in fact similar polarity patterns than that observed for family I events with only an opposite polarity for station

410   *MUNK*.

The performed analysis of fault instability clearly showed that high-quality focal mechanisms constituting family I events display comparable oblique reverse component and optimally oriented fault planes striking approximately NNW-SSE and dipping around 45°. These fault plane orientations are in agreement with the estimated stress field, and they explain well the spatio-temporal evolution of seismicity with corresponding fluid

415   migration pattern. The 2018 seismicity activated a pre-existing network of small-scale parallel fractures dipping to ENE, in agreement with the dip direction of the inclined part of the injection well. Fault planes striking NNE-SSW to NE-SW and dipping around 60° were also indicated to be quite favorably oriented with the stress field represented by the auxiliary plane of the mean FPSs for family I and III. Drill bit seismic data suggest the existence of a steeply dipping NE-SW striking structure which might be activated by the 2018 seismic activity. We note the

420   FM results are in good agreement with a limited number of 14 focal mechanisms of the strongest events presented in Hillers et al. (2020), which were all but one displaying reverse faulting motions.

14

5   Summary and conclusions

We present a new seismic catalog for the geothermal stimulation in Helsinki 2018 determining new locations and relocations on the basis of the new VSP-based velocity model and include the post-stimulation seismicity resulting in a catalog with 5,456 events. The catalog is extended by the list of detections, accounting to 61,163 events provided to scientific community (see section *data availability*). The magnitude of completeness of the entire catalog is $M_C = -1.10$. The catalog is supplemented by 191 focal mechanisms calculated using polarity-based and cross-correlation based methods and is used to discuss the structural complexity of the reservoir.

Spatial migration of the seismicity is driven by enhanced pore fluid pressure due to active injection, as no spatial migration of the post-stimulation seismicity after bleed-off is found. Until shortly after the bleed-off, the increase in the cumulative moment release of the post-stimulation seismicity with time is comparable with the slope of the CM_0 during individual stimulation phases but substantially less afterwards. This is especially observed for the seismicity of the deepest hypocenter cluster.

An activated network of at least three NW-SE to NNW-SSE oriented fracture zones of up to 200 m thickness seems to be responsible for the significant seismic activity migration towards NW-NNW and SE-SSE away from the injection well. The deepest fracture zone also hosts much of the larger seismic events with magnitudes exceeding $M_W \geq 1$, suggesting elevated fluid volume and pore fluid pressure, leading to accumulation of hydraulic energy in this area, relaxed in larger seismic events.

Best-constrained focal mechanisms strike NNW-SSE in agreement with orientation of three fracture zones. Most of these mechanisms display ~45° ENE dipping oblique-thrust fault planes that were found to be critically stressed in the resolved local stress field. These fault kinematics explains well NNW-SSE migration of seismicity along damage zones, as well as the downwards migration of events towards NE-NNE, along the dip direction vector of the inclined portion on injection well.

We conclude that seismic slip occurs on sub-parallel network of favorably oriented pre-existing but weak fractures, striking in NNW-SSE direction and dipping 45° ENE. The localization of seismic moment release in NNW-SSE trending zones suggest the existence of NNW-SSE trending damage structures or lithological differences that increase the mobility of fluids in this confined parts of the reservoir.

Data availability

The seismic event catalog with associated description of its basic statistical and spatio-temporal properties is available through GFZ data services: http://dataservices.gfz-potsdam.de/portal/ as a separate data publication. For

the event detections, the catalog contains origin times, local and moment magnitudes. For located events, the catalog contains origin times, local as well as moment magnitudes, absolute locations in local Cartesian coordinate system and for relocated events also the double-difference relocated locations in local Cartesian coordinate system. The fault plane solutions (strike, dip and rake) with associated uncertainties of estimated focal mechanisms are also included in the data catalog.

Competing interests

The authors declare that they have no competing interests.

Author contribution

M.L.: data reduction, analysis and results interpretation, draft version of the manuscript, and associated data publication. G.K. and P.M.-G.: data analysis, results interpretation, and manuscript correction. M.B., G.D., and P.H.: results interpretation and manuscript correction. T.S.: project management, drilling and stimulation program development and managing, and manuscript correction.

Acknowledgments

References

Ader, T., Chendorain, M., Free, M., Saarno, T., Heikkinen, P., Malin, P., Leary, P., Kwiatek, G., Dresen, G., Bluemle, F., and Vuorinen, T.: Design and implementation of a traffic light system for deep geothermal well stimulation in Finland, Journal of Seismology, https://doi.org/10.1007/s10950-019-09853-y, 2019.

Backers, T. and Meier, T.: Stress field modeling for the planned St1 Deep Heat geothermal wells for Aalto University, Finland, Report A1601/St1/160508fr, 2016.

475   Bentz, S., Kwiatek, G., Martínez-Garzón, P., Bohnhoff, M., and Dresen, G.: Seismic moment evolution during hydraulic stimulations, Geophysical Research Letters, 47, e2019GL086185, https://doi.org/10.1029/2019GL086185, 202019.

Bohnhoff, M., Malin, P., ter Heege, J., Deflandre, J.-P., and Sicking, C.: Suggested best practice for seismic monitoring and characterization of non-conventional reservoirs, First Break, 36, 2, 59-64, 2018.

480   D'Auria, L. and Massa, B.: Stress inversion of focal mechanism data using a bayesian approach: A novel formulation of the right trihedra method, Seismological Research Letters, 86, 1–10, https://doi.org/10.1785/0220140153, 2015.

Deichmann, N. and Giardini, D.: Earthquakes induced by the stimulation of an enhanced geothermal system below Basel (Switzerland), Seismological Research Letters, 80, 784–798,

485   https://doi.org/10.1785/gssrl.80.5.784, 2009.

Diehl, T., Kraft, T., Kissling, E., and Wiemer, S.: The induced earthquake sequence related to the St. Gallen deep geothermal project (Switzerland): Fault reactivation and fluid interactions imaged by microseismicity, Journal of Geophysical Research: Solid Earth, 122, 7272–7290, https://doi.org/10.1002/2017JB014473, 2017.

490   Efron, B.: The jackknife, the bootstrap, and other resampling plans, Siam, 1982.

Ellsworth, W.L.: Injection-induced earthquakes, Science, 341, 1225942, https://doi.org/10.1126/science.1225942, 2013.

Ellsworth, W.L., Giardini, D., Townend, J., Ge, S., and Shimamoto, T.: Triggering of the Pohang, Korea, earthquake (Mw 5.5) by enhanced geothermal system stimulation, Seismological Research Letters,

495   90, 1844–1858, https://doi.org/10.1785/0220190102, 2019.

Font, Y., Kao, H., Lallemand, S., Liu, C.-S., and Chiao, L.-Y.: Hypocentre determination offshore of eastern Taiwan using the maximum intersection method, Geophysical Journal International, 158, 655–675, https://doi.org/10.1111/j.1365-246X.2004.02317.x, 2004.

Galis, M., Pelties, C., Kristek, J., Moczo, P., Ampuero, J.-P., and Mai, P.M.: On the initiation of sustained slip-

500   weakening ruptures by localized stresses, Geophysical Journal International, 200, 890–909, https://doi.org/10.1093/gji/ggu436, 2015.

Giardini, D.: Geothermal quake risks must be faced, Nature, 462, 848–849, https://doi.org/10.1038/462848a, 2009.

Hanks, T.C. and Kanamori, H.: A moment magnitude scale, Journal of Geophysical Research: Solid Earth, 84,

505   2348–2350, https://doi.org/10.1029/JB084iB05p02348, 1979.

Hardebeck, J.L. and Michael, A.J.: Damped regional-scale stress inversions: Methodology and examples for southern California and the Coalinga aftershock sequence, Journal of Geophysical Research: Solid Earth, 111, B11310, https://doi.org/10.1029/2005JB004144, 2006.

Hardebeck, J. and Shearer, P.: A new method for determining first-motion focal mechanisms, Bulletin of the Seismological Society of America, 92, 2264–2276, https://doi.org/10.1785/0120010200, 2002.

Heidbach, O., Mojtaba, R., Reiter, K., Ziegler, M., and WSM Team: World stress map database release 2016 V.1.1, GFZ Data Services, https://doi.org/10.5880/WSM.2016.001, 2016.

Hillers, G., Vuorinen, T., Uski, M., Kortström, J., Mäntyniemi, P., Tiira, T., Malin, P., and Saarno, T.: The 2018 geothermal reservoir stimulation in Espoo/Helsinki, southern Finland: Seismic network anatomy and data features, Seismological Research Letters, 91 (2A), 770–786, https://doi.org/10.1785/0220190253, 2020.

Hofmann, H., Zimmermann, G., Farkas, M., Huenges, E., Zang, A., Leonhardt, M., Kwiatek, G., Martinez-Garzon, P., Bohnhoff, M., Min, K.-B., Fokker, P., Westaway, R., Bethmann, F., Meier, P., Yoon, K.S., Choi, J.W., Lee, T.J., and Kim, K.Y.: First field application of cyclic soft stimulation at the Pohang Enhanced Geothermal System site in Korea, Geophysical Journal International, 217, 926–949, https://doi.org/10.1093/gji/ggz058, 2019.

Kagan, Y.Y.: 3-D rotation of double-couple earthquake sources, Geophysical Journal International, 106, 709–716, https://doi.org/10.1111/j.1365-246X.1991.tb06343.x, 1991.

Kagan, Y.Y.: Simplified algorithms for calculating double-couple rotation, Geophysical Journal International 171, 411–418, https://doi.org/10.1111/j.1365-246X.2007.03538.x, 2007.

Kakkuri, J. and Chen, R.: On horizontal crustal strain in Finland, Bulletin Géodésique, 66, 12–20, https://doi.org/10.1007/BF00806806, 1992.

Kwiatek, G., Bohnhoff, M., Martínez-Garzón, P., Bulut, F., and Dresen, G.: High-resolution reservoir characterization using induced seismicity and state of the art waveform processing techniques, First Break, 31, 81-88, https://doi.org/0.3997/1365-2397.31.7.70359, 2013.

Kwiatek, G., Martínez-Garzón, P., Dresen, G., Bohnhoff, M., Sone, H., and Hartline, C.: Effects of long-term fluid injection on induced seismicity parameters and maximum magnitude in northwestern part of The Geysers geothermal field, Journal of Geophysical Research: Solid Earth, 120, 7085–7101, https://doi.org/10.1002/2015JB012362, 2015.

Kwiatek, G., Saarno, T., Ader, T., Bluemle, F., Bohnhoff, M., Chendorain, M., Dresen, G., Heikkinen, P., Kukkonen, I., Leary, P., Leonhardt, M., Malin, P., Martínez-Garzón, P., Passmore, K., Passmore, P.,

Valenzuela, S., and Wollin, C.: Controlling fluid-induced seismicity during a 6.1-km-deep geothermal stimulation in Finland, Science Advances, 5, eaav7224, https://doi.org/10.1126/sciadv.aav7224, 2019.

Lagarias, J.C., Reeds, J.A., Wright, M.H., and Wright, P.E.: Convergence properties of the Nelder--Mead simplex method in low dimensions, SIAM J. Optim., 9, 112–147, https://doi.org/10.1137/S1052623496303470, 1998.

Lomax, A.: A reanalysis of the hypocentral location and related observations for the great 1906 California earthquake, Bulletin of the Seismological Society of America, 95, 861–877, https://doi.org/10.1785/0120040141, 2005.

Lund, B. and Townend, J.: Calculating horizontal stress orientations with full or partial knowledge of the tectonic stress tensor, Geophysical Journal International, 170, 1328–1335, https://doi.org/10.1111/j.1365-246X.2007.03468.x, 2007.

Majer, E., Nelson, J., Robertson-Tait, A., Savy, J., and Wong, I.: Protocol for addressing induced seismicity associated with enhanced geothermal systems, US Department of Energy, DOE EE-0662, 2012.

Martínez-Garzón, P., Bohnhoff, M., Kwiatek, G., and Dresen, G.: Stress tensor changes related to fluid injection at The Geysers geothermal field, California, Geophysical Research Letters, 40, 2596–2601, https://doi.org/10.1002/grl.50438, 2013.

Martínez-Garzón, P., Kwiatek, G., Bohnhoff, M., and Ickrath, M.: MSATSI: A MATLAB package for stress inversion combining solid classic methodology, a new simplified user-handling, and a visualization tool, Seismological Research Letters, 85, 896–904, https://doi.org/10.1785/0220130189, 2014.

Martínez-Garzón, P., Vavryčuk, V., Kwiatek, G., and Bohnhoff, M.: Sensitivity of stress inversion of focal mechanisms to pore pressure changes, Geophysical Research Letters, 43, 8441–8450, https://doi.org/10.1002/2016GL070145, 2016.

Maxwell, S.-C., Shemeta, J., Campbell, E., and Quirk, D.: Microseismic deformation rate monitoring, in: SPE Annual Technical Conference and Exhibition, edited, pp. 4185–4193, Denver, Colorado: Society of Petroleum Engineers, 2008.

Nelder, J.A. and Mead, R.: A simplex method for function minimization, The Computer Journal, 7, 308–313, https://doi.org/10.1093/comjnl/7.4.308, 1965.

Rubinstein, J.L. and Ellsworth, W.L.: Precise estimation of repeating earthquake moment: Example from Parkfield, California, Bulletin of the Seismological Society of America, 100, 1952–1961, https://doi.org/10.1785/0120100007, 2010.

Shelly, D.R., Hardebeck, J.L., Ellsworth, W.L., and Hill, D.P.: A new strategy for earthquake focal mechanisms using waveform-correlation-derived relative polarities and cluster analysis: Application to the 2014

Long Valley Caldera earthquake swarm, Journal of Geophysical Research: Solid Earth, 121, 8622–8641, https://doi.org/10.1002/2016JB013437, 2016.

Tape, W. and Tape, C.: Angle between principal axis triples, Geophysical Journal International, 191, 813–831, https://doi.org/10.1111/j.1365-246X.2012.05658.x, 2012.

Vavryčuk, V.: Principal earthquakes: Theory and observations from the 2008 West Bohemia swarm, Earth and Planetary Science Letters, 305, 290–296, https://doi.org/10.1016/j.epsl.2011.03.002, 2011.

Vavryčuk, V.: Iterative joint inversion for stress and fault orientations from focal mechanisms, Geophysical Journal International, 199, 69–77, https://doi.org/10.1093/gji/ggu224, 2014.

Waldhauser, F. and Ellsworth, W.L.: A double-difference earthquake location algorithm: Method and application to the Northern Hayward Fault, California, Bulletin of the Seismological Society of America, 90, 1353–1368, https://doi.org/10.1785/0120000006, 2000.

Zhou, H.: Rapid three-dimensional hypocentral determination using a master station method, Journal of Geophysical Research: Solid Earth, 99, 15439–15455, https://doi.org/10.1029/94JB00934, 1994.

595

Figures

600 _____
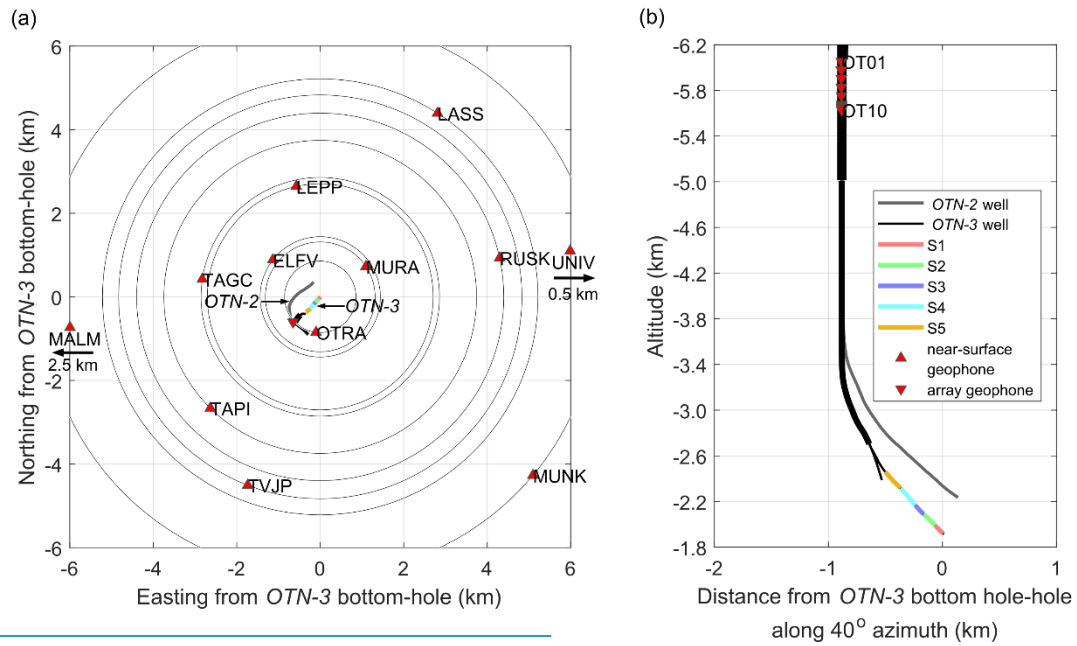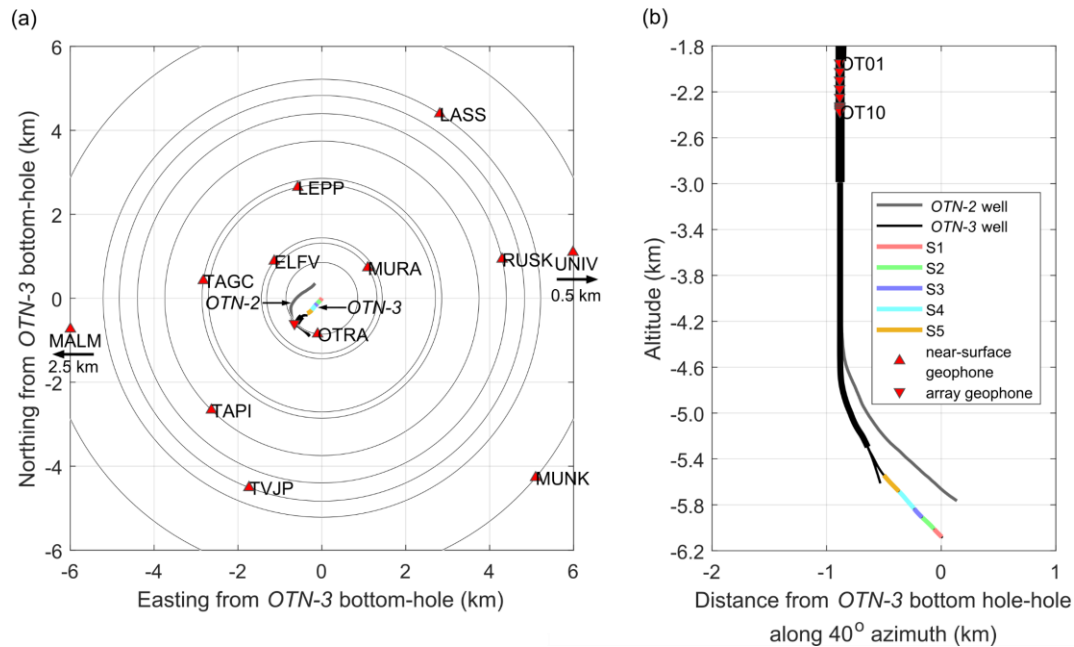
Figure 1. Seismic network used for monitoring the stimulation in 2018. (a) Map view showing the near-surface geophones framing the EGS site with the injection borehole *OTN-3* and the *OTN-2* well drilled in 2019 and 2020. Radius of concentric circles presents distance between the end of the *OTN-3* borehole and each station. (b) Side view of the boreholes with the geophone-array placed at the already existing part of the *OTN-2* well. The injection intervals S1-S5 of the stimulation in 2018 are color-coded at the end of the injection borehole. For further details about location of the EGS site at the suburban area of Helsinki in Finland see Kwiatek et al. (2019).

605
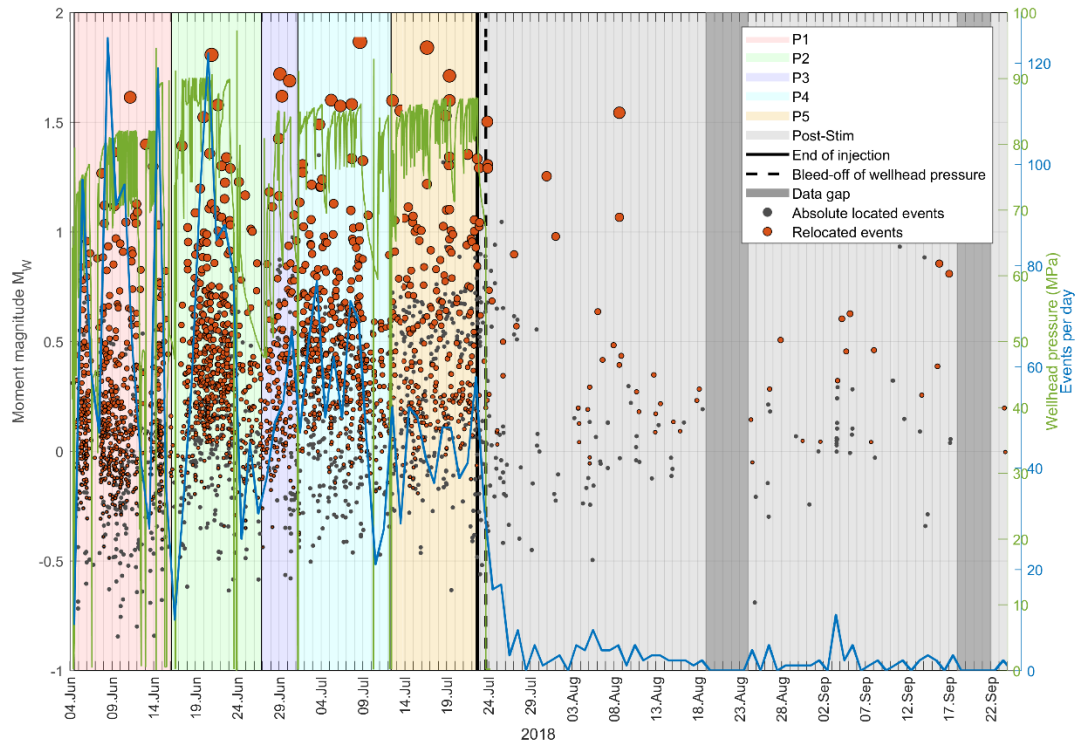
Figure 2. Stimulation protocol with moment magnitudes of induced seismicity during stimulation phases P1-P5 and post-stimulation time period. The magnitudes of 2,958 absolute located and 1,986 relocated events are shown as grey and orange dots, respectively. The green solid line presents the wellhead pressure during the stimulation. The seismic event rate per day is shown by the solid blue line.

(a)

(b)
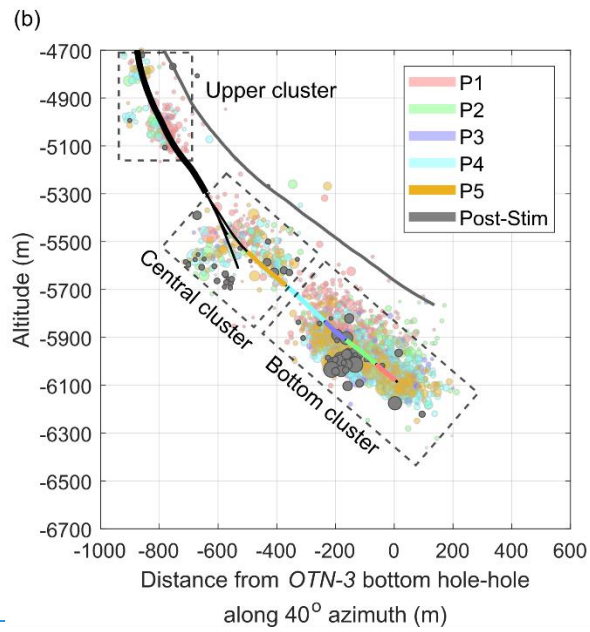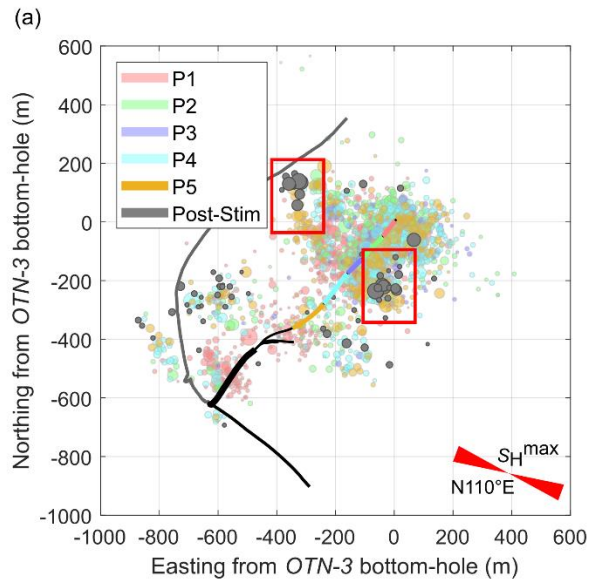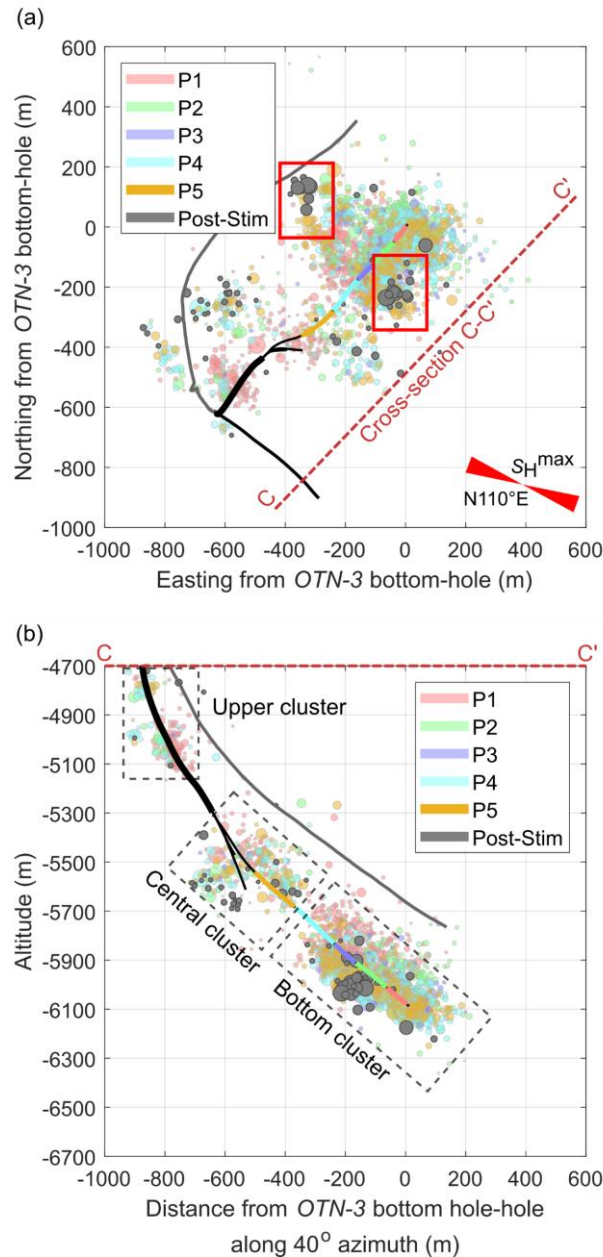
Figure 3. Hypocenters of relocated events. (a) Map view and (b) SW-NE depth section. The hypocenters are color-coded with the stimulation phases (cf. Kwiatek et al., 2019) and size corresponds to moment magnitude. Relocated seismicity that occurred after the stimulation is represented as grey dots. Areas with large events occurring during stimulation phase P5 and post-stimulation time are highlighted by red rectangles (see main text for details). The five injection stages are marked as color bands along the borehole trace from the bottom of the open-hole toward the casing shoe of the injection well *OTN-3* (black). The new *OTN-2* well (grey) was drilled in 2019 to 2020 after the stimulation.
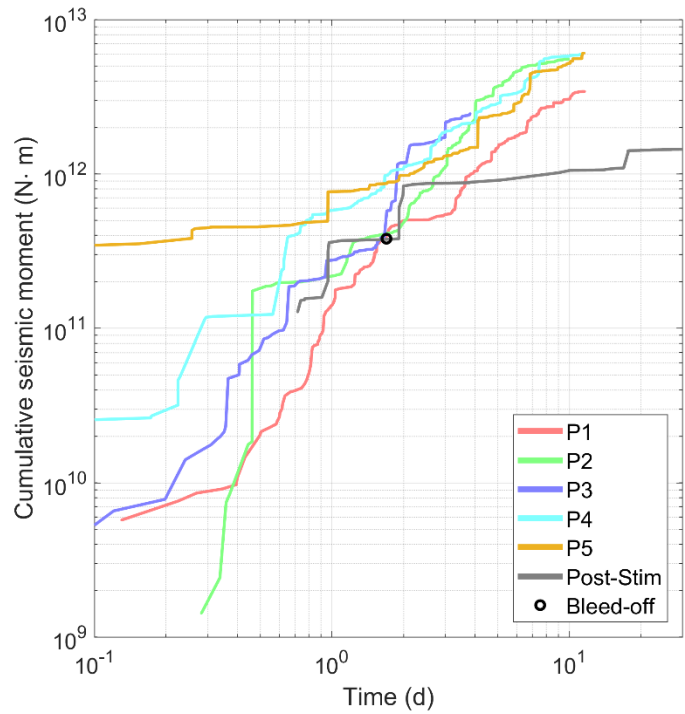
25

Figure 4. For a time period of 30 days, the temporal evolution of cumulative seismic moment release for the relocated seismicity is shown for each injection phase as well as for the post-stimulation phase.
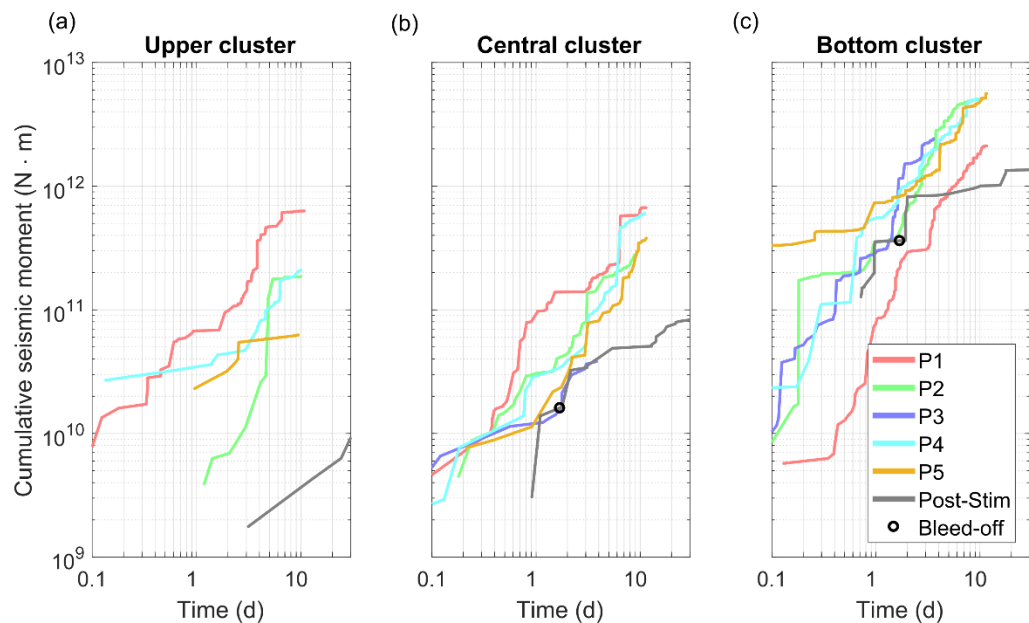
Figure 5. Temporal evolution of the cumulative seismic moment release with time for each of the three hypocenter clusters separately: (a) The uppermost hypocenter cluster, (b) the central hypocenter cluster and (c) the deepest and main hypocenter cluster.
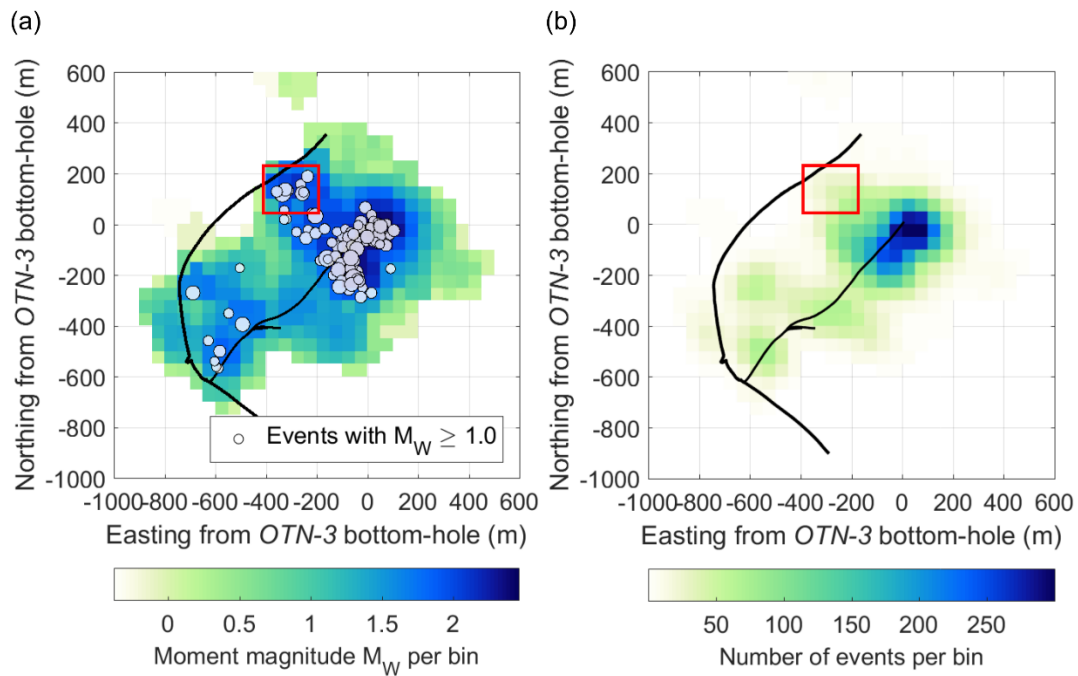
Figure 6. Spatial evolution of the cumulative seismic moment release of the relocated seismicity per bins of 50-by-50 m.
(a) The cumulative seismic moment release converted to seismic moment magnitude per bin overlaid by seismicity with $M_W \geq 1$. (b) The number of events that occurred per bin. A smaller area of anomalously high CM_0 release caused by a few large events is highlighted by red rectangle.
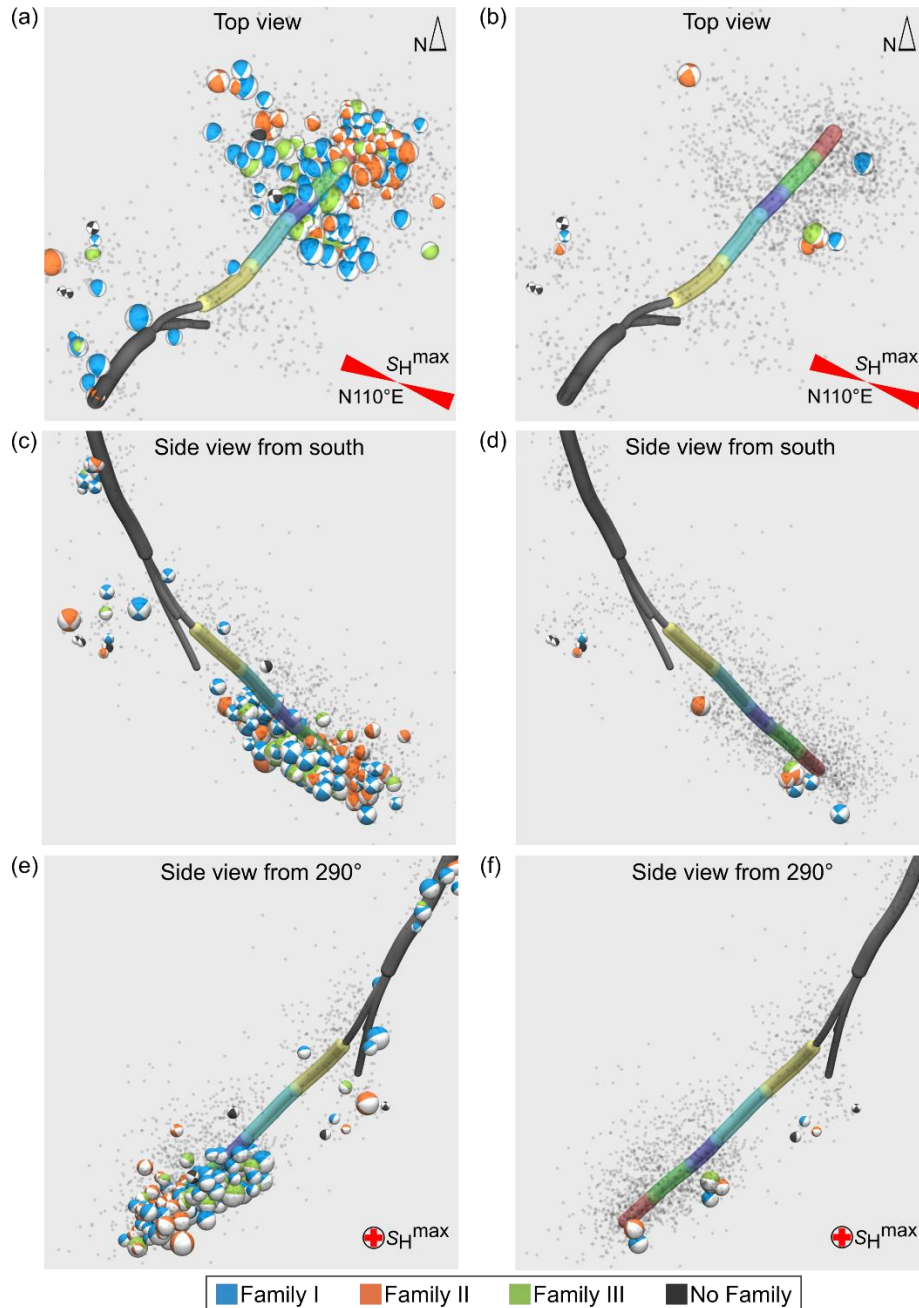
Figure 7. Orthogonal views of estimated focal mechanisms in three different projections: (a, b) map view, (c, d) side view from south (180°) as well as (e, f) side view from NW (290°), along the direction of the maximum horizontal stress $S_H^{max} = 110°$. (a, c, e): All 191 estimated focal mechanisms. (b, d, f): Focal mechanisms of post-stimulation events. Color-code indicating family obtained. Relocated seismicity without estimated focal mechanisms are plotted with grey small dots.
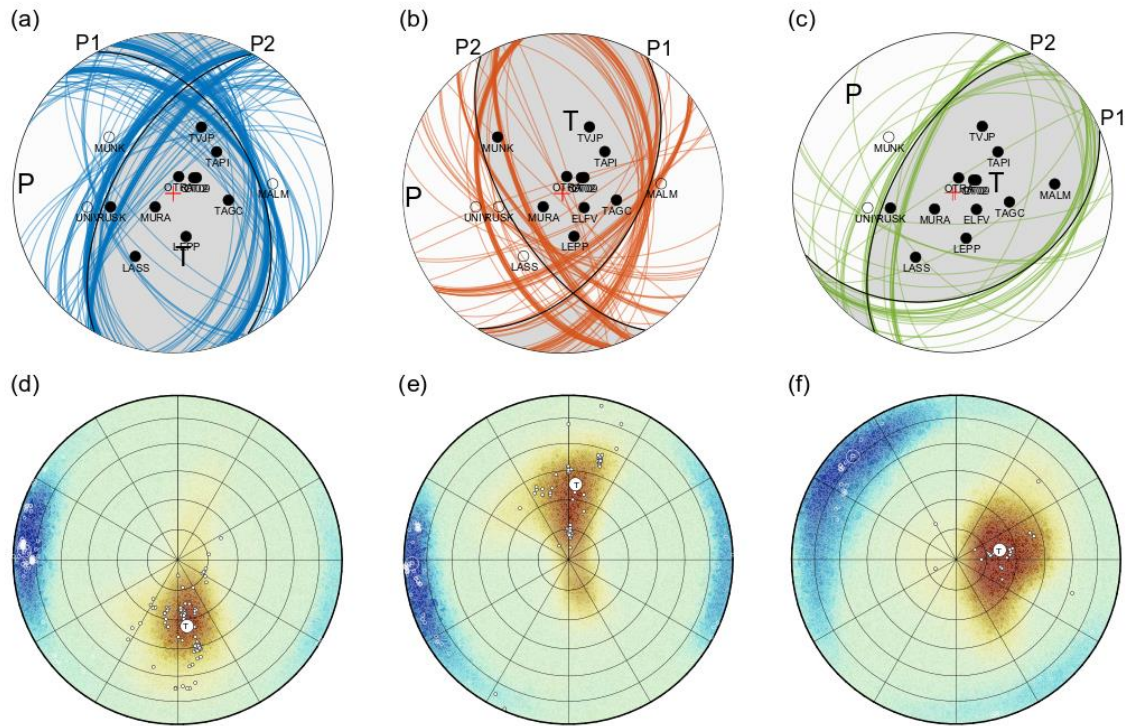
Figure 8. (a-c): Mean fault plane solutions (black lines) calculated from best FPSs of 99 events forming family I (a), 60 events forming family II (b) and 27 events forming family III (c). Contributing FPSs from which mean is calculated are shown with blue, orange and green color, respectively. The most repetitive polarity pattern observed at each station is presented as black or white dot for positive or negative onsets, respectively. P1 and P2 symbols correspond to the projections of main and auxiliary fault planes according to which one is better oriented for failure on the Mohr circle represented in Fig. 10. (d-f): For each of the families, the mean P- and T-axes as well as axes of contributing FPSs are plotted with big and small white dots, respectively. The *HASH*-derived uncertainties (95 % confidence interval) of the P- and T-axis of all events within each family are shown using blue and brown coloring scale, respectively.
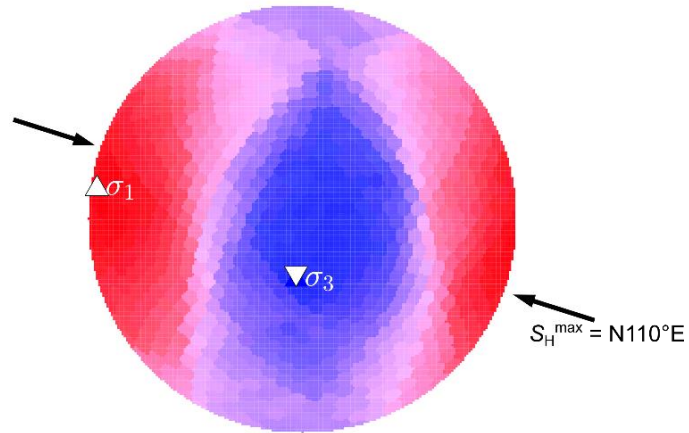
Figure 9. Stereonet of the estimated local stress field using *BRTM* method. White upward and downward pointing triangles represent maximum and minimum principal stress axes σ_1 and σ_3, respectively. Black arrows represent maximum horizontal stress S_H^{max} in the reservoir.

660
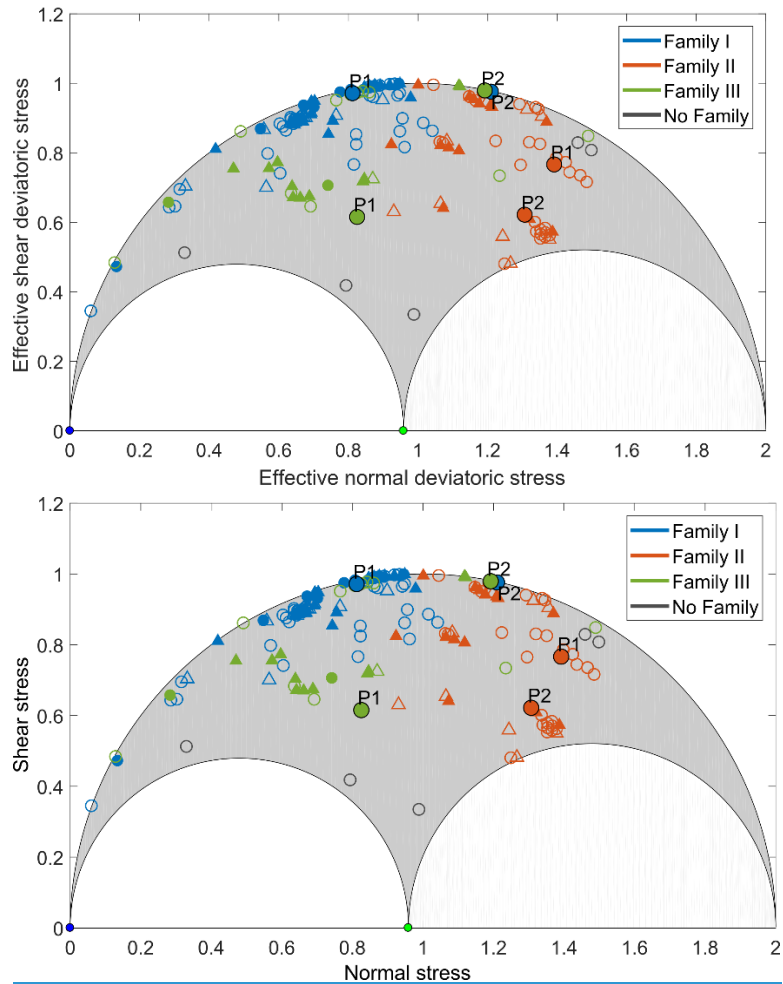
Figure 10. Deviatoric Mohr circle representing the local stress field with the fault plane solutions having the highest
fault instability coefficient of the estimated focal mechanisms. ~~The stress inversion resulted in a~~ A stress ratio of $R = 0.53$
~~was used for stress inversion~~. Events with $M_W \geq 1$ and $M_W < 1$ are plotted as triangles and circles, respectively. Filled
and unfilled markers represent events with manually picked and estimated polarities, respectively. The mean and its
auxiliary fault plane solution of each family are plotted as filled large dots labelled with P1 and P2, respectively. Most
family I events (blue symbols) occurred on critically stressed faults.
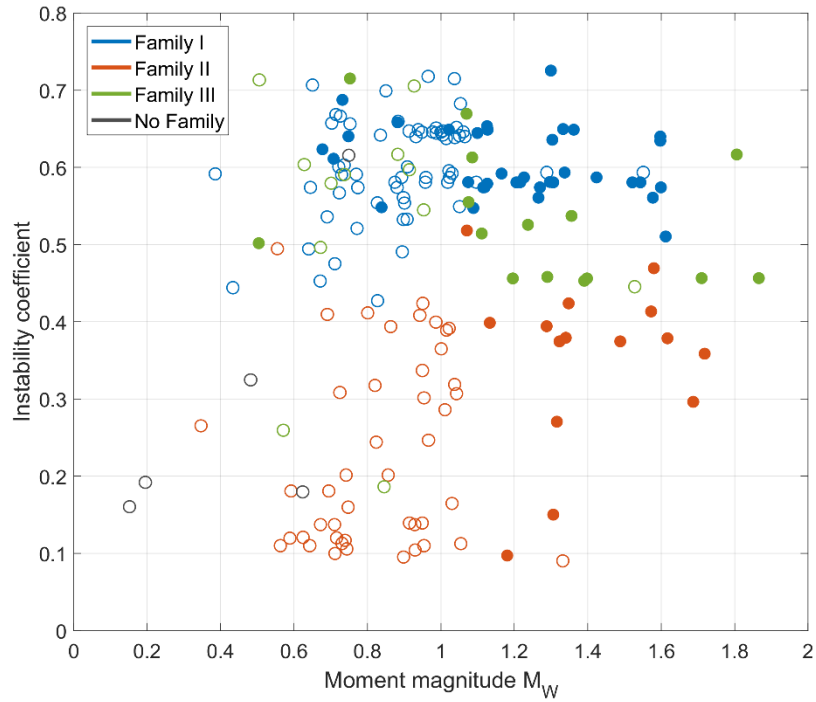
670

Figure 11. Highest fault instability coefficient of any of the two FPSs for each FM event plotted with moment magnitude. Events with manually picked and estimated polarities are plotted with filled and unfilled circles, respectively.

Tables

Table 1. Fault instabilities of mean fault plane solution and its auxiliary plane for each family.

	Instability of mean fault plane solution	Instability of mean auxiliary fault plane solution
Family I	0.6026	0.3978
Family II	0.1940	0.1629
Family III	0.4103	0.4087

675

33